PS

PPPL-3141 - Preprint Date: December, 1995, UC-420, 426

RECEIVED
MAR 13 1996
OSTI

FAST DETECTION OF 14 MeV NEUTRONS ON THE TFTR NEUTRON COLLIMATOR

S. von Goeler, A. L. Roquemore, L. C. Johnson,
M. Bitter, M. Diesso, E. Fredrickson, D. Long, and J. Strachan
Plasma Physics Laboratory, Princeton University
Box 451, Princeton, NJ 08543

Abstract: Current mode operation of the NE451 ZnS Scintillation Detectors of the TFTR Neutron Collimator has enabled us to record the development of radial neutron emission profiles with much faster speed and higher accuracy than in the pulse counting mode. During high-power DT operation, the intrinsic shot noise on the detector traces was so low that we could observe sawtooth instabilities and disruptions with good precision and, in addition, were able to identify precursor MHD activity and fishbone instabilities. These results demonstrate that in future tritium burning machines like ITER or TPX, the neutron collimator should be designed not only as a monitor of radial fusion power profiles but also as a wave detector for MHD activity.

MASTER

DISTRIBUTION OF THIS DOCUMENT IS UNLIMITED

I. INTRODUCTION

The main function of the Neutron Collimator[1,2,3] on the Tokamak Fusion Test Reactor (TFTR) has been the monitoring of the temporal development of radial profiles of the neutron emission from the hot plasma. The neutron profiles provide the experimental data on the fusion power density from the reactor. A very important result from TFTR - recently reported at the IAEA meeting at Seville[4] - consisted of Neutron Collimator data, showing that the fusion power density in the plasma core of TFTR during high power tritium shots exceeds the fusion power density projected for ITER, - relieving very much the fear that α-particle induced instabilities like TAE modes[5,6] pose a serious threat to plasma confinement. There are other interesting and useful data from the Neutron Collimator. The neutron emission in TFTR is due to beam-beam and beam-target interactions as well as collisions between thermal plasma ions. In general the beam-target fraction represents the largest component. Neutron profiles, therefore, provide an opportunity to check the theory of neutral beam deposition and slowing-down of the injected hot ions in collisions with the plasma electrons and ions,[7] and permit an estimate of the transport of hot ions. The onset of anomalous hot-ion transport - due to MHD instabilities - is often clearly distinguishable.[8] In the preceding examples, the neutrons diagnose the hot ions, and not the target. The opposite situation occurs during deuterium neutral beam injection into deuterium plasmas, when a tritium gas puff of very short duration is released into the discharge chamber near the plasma periphery. The inward transport of the thermal (target) tritium ions can then be followed, since the deuterium-tritium fusion cross section is so large that D-T neutrons represent the dominant component to neutron profiles.[9] This paper discusses a new application for the neutron collimator, the direct measurement of MHD instabilities.

NOTICE

Page(s) size did not permit electronic reproduction. Information may be purchased by the general public from the National Technical Information Service, U.S. Department of Commerce, Springfield, VA 22161 (Area Code 703-487-4650). DOE and DOE contractors may purchase information by contacting DOE's Office of Scientific and Technical Information, P.O. Box 62, Oak Ridge, TN 37831, Attn: Information Services (Area Code 423-576-8401).

Most of the results from the TFTR Neutron Collimator during deuterium operation have been obtained with the ZnS-based NE451 neutron detector system.[1,10] These detectors showed signs of saturation during DD injection with very high power, and saturated fully during DT operation. Therefore, a less efficient detector system, the so-called ZnS Wafer Detector System,[3] has been installed directly above the NE 451 system in the Neutron Collimator. It provides data during DT operation. Both systems have been operated in the past in the pulse counting mode. The primary cause for the saturation was pulse-pile-up.

The idea behind the work reported in this paper was to operate the saturated NE451 detector system in the current mode, where pulse-pile-up effects do not matter, in order to have a second, independent measuring system during tritium operation. In addition, the current mode provides a large improvement in time resolution. We were able with this system not only to follow closely the temporal evolution of the neutron emission during sawtooth instabilities and disruptions, but we could also see some of the precursor instabilities. We believe that the neutron collimator in future devices with tritium operation - for instance in ITER or TPX - should be laid out in such a fashion that it can serve as a wave detector similar to conventional soft X-ray Imaging systems.[11]

This paper is organized in the following way: In Section II we provide technical details of the current mode operation. We also briefly discuss the calibration of the current mode traces, and compare the current mode results with the pulse counting data from the wafer detector system. In Section III, we analyze the noise on the current mode signals and show that the noise is neutron shot noise. This is important for the construction of neutron collimators in future machines: They should be optimized to maximize the neutron flux intercepting the detector. In Sect. IV, we show examples of some of the data

that have been obtained with current mode operation of the NE451 system on TFTR. These include a sawtooth with fishbone precursor instabilities, a continuous m=2 MHD instability, and the famous (9.3 MW fusion power) disruption, TFTR shot #76778. Finally in Sect. V, we give a short summary and discuss the implications of our results for future devices.

II. Implementation of the current mode operation on the TFTR Neutron Collimator.

In this section, we discuss the technical details of the current mode operation of the TFTR Neutron Collimator. We start by giving a short description of the Neutron Collimator and its detector systems. Since detailed accounts of the collimator and its performance have already been presented in Refs. 1, 2, and 3, this discussion will be short.

A mechanical layout of the TFTR Neutron Collimator is shown in Fig. 1. 14 MeV neutrons from DT reactions or 2.5 MeV neutrons from DD reactions originate in the core of the TFTR plasma. The neutron source is observed through ten collimators of 51 mm diameter and approximately 400 cm effective length, which penetrate the 2 m thick concrete floor underneath the TFTR machine. There are four detection systems installed in a shielded enclosure in the TFTR basement: At a distance of 6.3 m from the horizontal mid plane of the plasma, the ZnS Wafer system (1) and the NE451 detector system (2), and at approximately 7.8 m from the mid plane, the ^{4}He detector array[12] and the Cotetra Neutron spectrometers[13]. The latter two arrays are designed to obtain information on the energy distribution of the neutrons.

We are here concerned mostly with the NE451 detector system that we use for the current mode. A detailed description of the detectors and their performance has been given in references 1 and 2. The detector consists of alternating, concentric, circular layers of clear plastic and of plastic in which zinc sulfide grains have been embedded. Incident neutrons produce recoil protons in the plastic, which hit the ZnS grains and generate short pulses of scintillation light. The plastic layer that contains the ZnS grains is opaque to light, and the layers of clear plastic allow the light to escape and reach a photomultiplier tube. The scintillations generate voltage pulses in the photo multiplier tube, which are counted by three independent scalers with three different thresholds. The wafer detector[3] works on the same principle, i. e. it is also ZnS recoil-proton detector; however, it employs only one thin (0.064") layer of clear plastic for production of recoil protons, and the ZnS consists only of a very thin (20 mg / cm^2) layer evaporated on one side of the clear plastic. Only those recoil protons which are born within a mean-free-path of the ZnS layer can produce scintillations. The wafer detector has consequently a much lower efficiency for neutron detection; most of the 14 MeV neutrons go just right through the detector without any reaction. The thinness of the clear plastic layer also reduces the sensitivity of the detector to γ rays. The Ne451 detectors saturate due to pulse-pile-up during deuterium-tritium operation, whereas the wafer detectors still perform satisfactorily, although - for shots with the highest power of neutral beam injection ($\approx$ 35 MW) and the largest neutron production - the count rate for the scaler with the lowest threshold reaches 2 MHz and we approach saturation.

Figure 2 shows a schematic of the signal processing electronics for the current mode, that was installed for the NE451 system. Neutrons stream down one of the collimator tubes and hit a NE451 detector. The scintillations of the ZnS

phosphor are detected by a photomultiplier (Hamamatsu R329). The multiplier base (Hamamatsu E934) contains only resistors and capacitors and no nonlinear elements, so that the high voltage can be changed with out affecting the voltage ratios of the dynodes, if the photomultiplier current is sufficiently small compared to the current in the resistor string. A standard, remotely controlled Ortec power supply provides the high voltage. The next element in line is a switching box, which is remotely controlled via CAMAC and allows us to switch from current mode to pulse counting mode in the middle of a run, from the TFTR control room. There is a small resistance in the contact of the TELEDYNE 712D-26 solid state relays, which causes a 3% reduction of the pulse height. In principle, the 3% reduction can be compensated for by a small high voltage increase. The scaler branch contains standard electronics described in Ref. 1. The current mode branch contains an array of current amplifiers, PPPL/E1520, which consist of (somewhat outdated) home-made X-ray imaging amplifiers, which we used simply because they were available. The bandwidth of the current amplifiers was restricted to 40 kHz in a crude fashion by placing a suitable capacitor across the 500 kΩ feedback resistor of the amplifier, in order to match the sampling frequency of the BIRA 908 transient digitizers, normally operated at a 40 kHz clock rate. Ideally, the bandwidth of the amplifiers should be limited to the Nyquist frequency, and an array of 5-pole 20 kHz low-pass filters is under construction and will be installed in the near future.

For DT shots, the rate of neutrons that hit a detector increases by a factor of more than 100 over those measured in DD discharges. Although the BIRA digitizer has 12 bit resolution, there exists a dynamic range problem. This was solved by automatically switching the high voltage on the photomultipliers to a lower value during the tritium shots, using a tritium flag set in the neutral beam injection computer control system. Actually, the high voltage of the

central channels during tritium operation is only 650 Volts, an uncomfortably low value for 12 stage photomultipliers. Since the amplifier gain is never changed, the high voltage determines the anode current in the photomultiplier, which is smaller than 20 μA.

In 1993 an absolute calibration of the NE451 detector system operating in pulse counting mode was performed using an in-situ 14 MeV neutron generator inside the TFTR vacuum vessel.[12] Subsequently, after the installation of the ZnS wafer detector system, a cross calibration of the two system was performed. The calibration of the current mode system has been accomplished in a very simple fashion by transferring the calibration of the ZnS Wafer detector system back to the NE451 current mode signals. Since both detectors sit right on top of each other in the same collimator tube, they sample the same neutron flux. Figure 3 shows such a comparison. The heavy solid lines represent the NE451 current mode traces , rebinned to a sampling frequency of 1.25 kHz. The thin lines, which are considerably more noisy, represent the output from the ZnS Wafer detector system, rebinned to a sampling frequency of .25 kHz. In order to facilitate the comparison, the current mode traces are multiplied with a "calibration factor" f_{cal} that is printed on the left side of the graph for each curve; f_{cal} is obtained by comparing the average intensity for each of the traces in the calibration time interval indicated by the dashed horizontal line at the bottom of the graph. The factor f_{cal} should be the same for different shots and should be independent of the choice of the calibration time interval, as long as the high voltage on the photomultipliers is not changed. We find that f_{cal} is identical within 1 or 2% in discharges that are similar. For instance, in Table 1 we list the calibration factors for two channels, obtained for a series of similar shots on a single day.

Table 1: fcal for DT shots on Nov. 4, 1994.

SHOT #	CHAN. #5	CHAN. #6
80654	159.4	95.3
80655	160.9	95.8
80707	160.1	94.7
80708	157.2	94.9

However, for discharges that are very different, there are deviations at the 5 to 10 percent level. These 5 to 10% deviations do sometimes occur in the course of a single discharge, as illustrated in Fig. 3 by the traces of the ZnS wafer and the NE451 detector for channel #5 (R=2.47 m). In this particular case, the cause for the deviation is known. The central ZnS wafer detectors operate in very high power discharges near the upper limit of their count rates, and there are signs of saturation due to pulse pile up for the wafer detector in channel #5. This is, however, not the explanation for all the observed deviations. The response to low energy neutrons, for instance, is very different for the two systems, and the wafer detector has a much smaller sensitivity to scattered neutrons than the NE451 detector in current mode (see discussion on the scattered neutron correction further down). These and other effects are under investigation, and the exact cause for the observed discrepancy between the two measurments is not clear in all cases.

Some uncertainties in the measurement are produced by (a) secondary neutrons and gamma rays, and (b) scattered neutrons. Secondary neutrons and gamma rays are produced when the 14 MeV neutrons from the plasma core hit the walls of the collimator tube. Computer simulations, assuming that a collimator channel consists of a steel tube surrounded by concrete, indicate that

about 16 percent of the neutrons, which hit the wafer detector and the Ne451 detector are secondary neutrons[14]. Of these, 63 % have energies between 5 and 14 MeV, the remaining 37% have less than 5 MeV energy. The gamma flux produced by the 14 MeV neutrons amounts to 6.7% of the total neutron flux, and most of them have energies above 1 MeV. Basically, the secondary neutrons cause a serious problem only for the absolute calibration because their signal is proportional to the primary 14 MeV neutrons. They can also cause cross talk among channels, and make contributions to noise.

Turning now to effect (b): Scattered neutrons are produced by the 14 MeV neutrons hitting the TFTR vacuum vessel walls or TF coil structure in the view of a collimator tube. The stainless steel vacuum flanges in the view of the neutron collimator (both on the bottom and on the top of the vacuum vessel) have been thinned to 3 mm in order to reduce the number of scattered neutrons. Still, the scattered neutrons can make a contribution, especially on the outer collimator channels, where the direct neutron signal is small. The size of the scattered neutron signal can be estimated from experiments with very small plasmas on the inboard or outboard limiter, where the outer channels are not intercepting any closed flux surfaces. The same procedure[2], that had been developed for the ZnS Wafer detector system, is used to subtract a scattered neutron correction from the current mode data. This procedure, which is described in detail in Ref. 2 and 3, subtracts a small signal proportional to the general total neutron yield, e. g. a U235 fission detector signal, from the trace of a collimator detector; the proportionality constant depends on the distance of the line of sight to the measured center of the plasma according to a semi-empirical formula. Figure 4 shows an example: The dotted curves in Fig. 4 are the raw data from each channel. The dashed curves represent the scattered neutron contribution derived from the fission chamber NE-CU-S3, the solid

curves are the corrected curves after the subtraction of the scattered neutron contribution. For the central four channels, which are usually the important contributors to the neutron profiles, the scattered neutrons account for less than 16% of the signal, and for the two central channels for less than 5% of the signal. For the four outer channels, the correction amounts normally to twenty to sixty percent, and for the channel at R= 3.32 m to eighty or ninety percent. The traces from this channel look very similar to the total neutron signals on TFTR.

The pulse counting mode is considered superior to the current mode for the rejection of scattered neutrons and gamma rays, since it employs an energy threshold to discriminate against the slower scattered neutrons. Therefore, the use of the same subtraction procedure for the current mode and the pulse counting is only approximately valid. The justification comes from two facts: (a) For the central channels the scattering correction is small, and practically insignificant, whereas for the outer channels the measured neutron signal is small, and the size of the correction usually does not affect the total neutron yield or the shape of the neutron profile very much. (b) The time behavior of the output signal of the wafer detector is observed to be the same as that of the Ne451 detector in current mode, within 10%. However, we should point out that there is room for inaccuracies within those 10%. Since the wafer detector traces are very noisy, especially for the outer channels, the accuracy of the wafer detector measurements itself is not much better than 10%, unless one integrates over the whole shot or a long time period.

There is considerable statistical noise on the fission detector traces, and the scattered neutron correction procedure consequently introduces noise on the corrected current mode traces. For neutron fluctuation measurements the

exact shape of the neutron emission profile and its development are often not of paramount importance. For neutron fluctuations, we have simplified the problem somewhat by assuming that the scattered neutron correction does not change with time during a shot; we then define a scattered neutron reduction factor ($1\text{-}fr_{sct}$) with which we simply multiply the raw data in order to obtain the plasma source neutron traces. fr_{sct} is the scattered neutron fraction derived from the fission detector and averaged over the whole shot. This procedure minimizes the noise. The factor ($1\text{-}fr_{sct}$) is printed out in Fig. 4 at the upper left hand corner of each of the graphs for the 6 different channels .

III. Noise on the current mode traces of the TFTR Neutron Collimator.

Signals from the NE451 detectors in current mode with a 40 kHz sampling rate exhibit noticable noise on all traces, which has the following properties: The noise increases and decreases as the signal increases and decreases, the noise is smaller for the central channels, which have more incident neutrons, and larger for the outer detectors with smaller neutron signals. These features suggest that the noise on the traces is neutron shot noise, i.e. noise caused by the statistical arrival of neutrons. As we will see later in Section 4, there are often MHD instabilities mixed in with the noise. However, there are many shots where there is no MHD activity noticable on the collimator traces, among them shot #80483, which has been shown in Fig.3 and will serve now as an example for the noise discussion throughout this section.

In order to test the neutron shot noise hypothesis more quantitatively, we have compared the noise on the traces of the NE451 detectors with theoretical predictions. We are using two computer programs to analyze the noise.

The first program is called NOISE. As a first step, NOISE rebins the data taken with 40 kHz sampling frequency to 20 kHz in order to eliminate the effect of the anti-aliasing filter. Then Noise fits a straight line, y_{fit}, through consecutive bins of 64 data points and determines the mean square deviation of the data from the line fit,

$$\sigma^2 = \frac{1}{64}\sum_{k=1}^{64}(y(t_k)-y_{fit}(t_k))^2 .$$

We have chosen this algorithm -in contrast with e. g. a simple deviation from a mean - in order to avoid errors that are generated at the begining or at the end of neutral beam injection, when the steep rise or fall of the neutron signal would mimic false noise signals. The program plots the experimental signal to noise ratio SNR versus time

$$SNR_{exp} = \frac{\langle y \rangle}{\sigma},$$

where <y> is the signal average over the time slot of 64 data points. The SNR signals for shot #80483 are plotted versus time in Fig. 5. The signal over noise ratio is about 100 for the central channels, and decreases dramatically for the outer channels where fewer neutrons are registered. Also shown in the figure are theoretical calculations of neutron shot noise (dashed curves). For the computation of these curves, the number of neutrons r_n passing per second through the NE451 detector is calculated, using the calibration described in Sect. II. The average number of these neutrons in a sampling time interval τ_s is then $\bar{N}_s = r_n \tau_s$. The standard deviation for random arrival is $\sigma = \sqrt{\langle (N_s - \bar{N}_s)^2 \rangle} = \sqrt{r_n \tau_s}$, and the signal over noise ratio for pure neutron shot noise SNR_{nsn}, should consequently be

$$SNR_{nsn} = \frac{\bar{N}}{\sigma} = \sqrt{r_n \tau_s} .$$

Of course not all neutrons that pass through the detector interact with the detector, and , in addition, they do not produce pulses of equal height but

rather a whole spectrum of pulses (even if all the neutrons had the same energy). The noise in the detector is consequently larger, and the measured SNR of a detector is smaller. A theoretical treatment for these effects will be given later at the end of this section. Here, we consider it an experimental problem and determine the ratio of the theoretical signal over noise SNR_{nsn} to the measured signal over noise SNR_{exp}, and call this ratio the experimental noise factor NF_{exp},

$$NF_{exp} = \frac{\langle SNR_{nsn} \rangle}{\langle SNR_{exp} \rangle}$$

The brackets indicate averaging in the time interval, where the comparison is made. The noise factor is considered a detector property, which should be independent of the of the choice of comparison time interval. In Fig. 5 the dashed curves represent the quantity SNR_{nsn} / NF_{exp}, where the noise factor NF_{exp} was computed in the time range from 3.35 to 3.55 sec, indicated in the figure by the horizontal bar above the time axis. The noise factor NF_{exp} is printed out at the upper left corner of the graphs for each channel. It is not surprising that the theoretically calculated dashed curves agree with the experimental curves in the time range 3.35 to 3.55 sec, because the factor NF_{exp} was chosen so that the two curves fall on top of each other in the comparison interval. However, the fact that the two curves agree for the whole shot, indicates that we are indeed dealing with neutron shot noise. The experimental noise factor is not the same for all detectors, but varies from detector to detector. This behavior is probably genuine. The detectors in channnels #3, #5, and #6 (at radius R = 2.08, 2.47, and 2.68 m) stem from a different batch in the manufacturing process, and have a lower noise factor. Channel #9, and also #2, (at 1.94 and 3.32 m) have also a lower noise factor. This is the case because the signal has a large scattered neutron contribution for the outer traces, and scattered neutrons have not been taken into consideration in the present noise analysis.

The second noise analysis program is called "FOURIER", and it was written to see whether the noise is indeed white noise. FOURIER plots the Fourier spectrum of the signal for a given time interval. An example is shown in Fig. 6. A fast Fourier transform is performed in the time interval from 3.500 to 3.532 sec containing 1536 sample intervals, and the absolute value of the Fourier spectrum is divided by the average of the signal, and multiplied with the square root of the Fourier time interval (38.4 msec). The latter operation is performed so that the result becomes independent of the length of the Fourier interval, and equals the square root of the so-called Wiener power spectrum (i.e. power per frequency interval). The Fourier transform data have been smoothed over 7 data points. For white noise we expect a flat spectrum which droops slightly near the Nyquist frequency (20 kHz) because of the anti-aliasing high frequency cut-off of the current amplifier. The measured spectra in Fig. 6 are relatively flat, although there is a slight droop that is not fully understood. One possible cause for the droop could be the decay of the ZnS phosphor, although we would expect a much smaller droop. The data are again compared with theoretical curves. First we consider pure neutron shot noise, which will produce a flat spectrum, which has a value $FT_{nsn} = |S(f)|/S$ according to Rice[15]

$$FT_{nsn} = \frac{1}{\sqrt{r_n}}.$$

As previously, we define a noise factor, NF_{exp} by averaging the measured Fourier transforms over frequency and dividing the average by the theoretically predicted pure neutron shot noise. In Fig. 6 the neutron shot noise calculations, $FT_{nsn} \times NF_{exp}$, are represented by the dashed curves, and the experimental noise factor NF_{exp} is listed in the uper left corner for each channel. The

exact value for the noise factor depends on the frequency range in which the comparison is made. Because of the droop, NF_{exp} will be smaller if the comparison is made at higher frequencies. Therefore, we have listed not only the value obtained by averaging over the whole frequency range (1.88 - 20.0 kHz), but also another number in brackets that pertains to lower frequencies (1.88 - 5.0 kHz). In both cases frequencies below 1.88 kHz were excluded, because this range contains the frequency components associated with the time change of the neutron emission and has nothing to do with shot noise. The general trends that the noise factor exhibits are the same that we encountered in the NOISE analysis (FIG. 5): The detectors in channel #3, 5, and 6 are from a different batch and have lower noise than channel #4, 7, and 8. Channel #9 has lower noise because the scattered neutron correction was not properly taken into account. The noise factors from the NOISE program come out somewhat higher than the full-range NF_{exp} values from the Fourier program, which is to be expected, because NOISE does not distinguish between frequencies and the lower frequencies give a stronger contribution.

As a final step we have tried to develop a quantitative theoretical explanation for the noise factor. The detector, exposed to the neutron flux, will produce a pulse height spectrum F(E) that is proportional to the neutron flux, i.e. the number of pulses with energy or pulse height E in the energy interval [E , E+dE] is assumed to be F(E) dE. We can consider all the events with the same pulse height as an individual random process. Later then, we will add up the various random processes with different pulse height. The mean, variance, amplitude of the power spectrum and relative Fourier noise amplitude of a random process $z(t)=\sum_{j=1}^{K}\delta(t-t_j)$ is, as we discussed before,

$$\langle z(t)\rangle = r \qquad \sigma^2 = r\tau \qquad S(\nu) = r \qquad s_z(\nu) = \frac{\sqrt{S_z(\nu)}}{\langle z\rangle} = \frac{1}{\sqrt{r}},$$

All pulses with equal pulse height form a random process $z(t) = E\sum\delta(t-t_j)$ with rate $r = F(E)dE$, and the mean, variance, and power spectrum are given by

$$\langle z_i \rangle = E_i\, F(E_i)\,\Delta E \quad \sigma_{z_i}^2 = E_i^2\, \tau\, F(E_i)\,\Delta E \quad S_i(\nu) = E_i^2\, F(E_i)\,\Delta E$$

The average, variance, and power spectrum for the whole process can simply be obtained by summation (central limit theorem)

$$\langle z \rangle = \sum_{i=0,}^{n} \langle z_i \rangle = \sum_{i=0,}^{n} E_i\, F(E_i)\Delta E = \int_0^{E_{max}} dE\, E\, F(E)$$

$$\sigma_z^2 = \sum_{i=0,}^{n} \langle \sigma_{z_i}^2 \rangle \tau = \sum_{i=0,}^{n} E_i^2\, \tau F(E_i)\Delta E = \tau \int_0^{E_{max}} dE\, E^2\, F(E).$$

$$S_z(\nu) = \sum_{i=0,}^{n} \langle S_{z_i} \rangle = \sum_{i=0,}^{n} E_i^2\, F(E_i)\Delta E = \int_0^{E_{max}} dE\, E^2\, F(E)$$

The rate of neutrons passing through the detector is r_n. F(E) will be proportional to r_n with the proportionality constant $\eta(E) = F(E) / r_n$, where η represents the number of pulses per unit energy for one incoming neutron. The relative noise for the total process is then given by

$$|s(\nu)| = \frac{\sqrt{S_z(\nu)}}{\langle z \rangle} = \frac{\sqrt{r_n \int_0^{E_{max}} dE\, \{E^2\, \eta(E)\}}}{r_n \int_0^{E_{max}} dE\, \{E\, \eta(E)\}} = \frac{1}{\sqrt{r_n}}\, NF,$$

i.e. the noise factor obeys the formula

$$NF = \frac{\sqrt{\int_0^{E_{max}} dE\, \{E^2\, \eta(E)\}}}{\int_0^{E_{max}} dE\, \{E\, \eta(E)\}}$$

In order to obtain a value for the noise factor NF, we have measured the pulse height spectrum produced in a spare Ne451 detector by the 14 MeV neutrons from a DT neutron generator[16,17] at a distance R from the detector. The neutron source strength of the generator was calibrated using the activation of aluminum foils.[18] Figure 7 shows the measured pulse height spectrum produced by the DT neutron generator. Plotted is the number of pulses per incoming neutron versus channel number. The noise figure NF for the detector, using the above formulae, is 4.811. A characteristic feature of this spectrum of

the NE451 detector is the very large amount of very low energy pulses. The low energy pulses occur just above the general noise from the multiplier tube, and consequently are hard to determine accurately. Because of the large number of low energy pulses and the steepness of the spectrum, the noise factor depends sensitively on the exact shape of the spectrum in that region. The spectrum shown is actually a composite of several spectra, where we have increased the gain and the high voltage on the photomultiplier tube - always subtracting a background spectrum with the neutron generator turned off - , in order to obtain a better estimate of the spectrum in the low energy region. The noise factor determined in this fashion is accurate only within 20 ... 30%. It is of the same magnitude as the experimental noise factor measured on TFTR in DT discharges. Consequently, it is likely that the noise seen on the traces in Fig. 5 and Fig. 6 is indeed caused by 14 MeV neutron shot noise.

Let us conclude this section by discussing the capability of the present NE451 system, and answer the question "What is the minimum detectable fluctuation level"? The relevant numbers for the four central collimator channels are put together in Table #2 for a discharge with very low noise, the shot with the highest DT fusion power (10.7 MW) in TFTR at the time of the maximum of the neutron emission.

Table #2: Fluctuation Detection Levels for Shot #80539

Channel	#4	#5	#6	#7
Radius [m]	2.23	2.47	2.68	3.00
Neutron Rate r_n	1.2×10^9 n/s	4.0×10^9	7.4×10^9	1.0×10^9
SNR_{nsn} /NF_{exp}	36	90	113	34
$FT_{nsn} \times NF_{exp}$	0.00013	0.000053	0.000042	0.00013

The neutron rate shown in the third row of Table #2 represents the number of 14 MeV neutrons that pass through the detector per unit time. For the calculation of the fourth and fifth row, we assumed that the sampling frequency is 40 kHz, and took the noise factor from Figs. 5 and 6. For the central channels an oscillation of the neutron emission would have to have an amplitude of 1%, in order to compete with neutron shot noise. However, the traces can be smoothed, and hence we were able to detect fluctuations with amplitudes of a fraction of a percent on the central collimator channels. The fifth row seems to indicate that much smaller amplitude fluctuations should be detectable, if one uses Fourier analysis. However, the numbers shown are good only for oscillations that last a second and do not change their frequency during this time. Usually, MHD precursor fluctuations last only for a few milliseconds, and if they stay for longer times they change frequency. We consequently performed the Fourier analysis normally for 128 data points, i. e. a time interval of 3.2 msec, and the numbers in the fifth row have to be multiplied with a factor of $\sqrt{1/0.0032} = 17.7$, in order to represent realistic estimates. This means , that the detection level - using Fourier analysis - is about 0.2 % on the central channels for high power DT discharges. Therefore, our technique has been to perform a fast Fourier transform, as shown in Fig. 9, and then, knowing the frequency of the instabilities, to use digital filters (mostly low pass filters, but sometimes also band pass filters) to prepare and compare traces, and to determine the relative phasing of the MHD oscillations on different channels.

IV. The TFTR Neutron Collimator as a wave detector.

In order to demonstrate the performance of the neutron collimator current mode, we want to show now several examples of neutron traces that have been obtained during deuterium tritium operation on TFTR during the year 1994.

We will show data from discharges with sawteeth, with fish bone instabilities, with a continuous m=2 oscillation and a major disruption. None of the observations reported in this section - except perhaps the inverted sawteeth seen in the discharge with the continuous m=2 instability - represents unexpected new physics. New is that these phenomena have been observed on collimated neutron traces. Since the neutrons intensity is predominantly due to beam target reactions and depends consequently very strongly on the fast ion component in the plasma from the neutral beam, a detailed analysis might show that the neutron signals also carry new physics information, however, at the present time this analysis has not been performed.

First we show data from a sawtooth discharge, plasma shot #80478. The line-integrated neutron emissivity of the six central collimator channels is shown in Fig. 8. Three sawtooth events[19] are clearly distinguishable at times 3.48, 3.79, and 4.02 sec. The neutron intensity in the two central channels (R = 2.47 and 2.68 m) decreases, whereas the intensity in the outer channels (particularly at R=2.23 and 3.00 m) increases, a behavior commonly seen on soft X-ray, plasma density and ECE electron temperature traces. For the outermost channels, in particular for R = 2.08m, the rise is very slow, and the maximum of the rise occurs only 20 ms after the sawtooth crash at time 3.796 sec. This behavior again closely resembles the time evolution of the soft x-rays during sawteeth, and is called heat pulse propagation[20,21]. The new information is that we are observing the heat pulse on the neutron emission, which might allow us to estimate the transport of fast ions during the sawtooth disruption. The six central traces are expanded in time at the bottom of Fig. 8. Obviously an instability occurs before and right through the saw tooth crash. It is particularly strong on the channel at R = 2.47 m. This is the well-known fishbone instabilities[22,23], a MHD instability with poloidal and toroidal mode numbers

m=1, n=1, which is driven by the interaction of the fast ion component from neutral beam injection with an m=1, n=1 internal kink instability [24,25]. Actually, the trace at R = 2.47 m shows that the sawtooth crash is preceded by a large number of fish bone bursts. This can be seen better in a contour plot (Fig. 9), where the Fourier amplitude is plotted versus time and frequency. The sawtooth at time 3.795 sec as well as the sawtooth at time 4.022 sec are preceded by a series of fishbone bursts with frequency of approximately 2.8 kHz. The fishbone instability slows down in frequency shortly before the sawtooth to approximately 1.8 kHz right at the time of the sawtooth crash. The details of the final sawtooth development are shown in Fig. 10 for the four central channels of the collimator . The 1.8 kHz precursor oscillations at R = 2.68 m have the opposite phase of the oscillations at R =2.47 m, demonstrating that the poloidal mode number of the instability is odd (i. e. m=1).

On TFTR, fishbones are frequently not associated with a sawtooth disruption, but occur by themselves. However, they still cause a deterioration of the neutron profile. Figure 11 shows the two central neutron traces and the neutron peakedness for shot #80482 during the onset of fishbone instabilities. The fishbones are clearly visible on the trace for R=2.47 m. Each fishbone causes a tiny sawtooth-like dip on the trace for R = 2.68 m, and a tiny inverted sawtooth on the trace for R=2.47 m. As the trace for the neutron peakedness indicates, the profile tries to recover after each burst, but looses more of its peakedness in the next burst. It is possible that the fishbones are responsible for the roll over of the neutron emission in this shot. In this case the roll over and the deterioration of the profile is so gradual that there might have been other forces at work. However, the deterioration often sets in very suddenly and is accompanied by a rapid onset of strong fishbones, so that instability and the profile deterioration are linked. The deterioration of the neutron profile dur-

ing fishbone activity is substantial, but usually not catastrophic.

We now discuss two other MHD phenomena that have been observed on the TFTR neutron collimator, namely a continuous m=2 instability and an inverted neutron saw tooth. Both features have been seen in the same discharge (shot #79092). Neutron collimator traces for this shot are shown in Fig. 12. A Fourier analysis as in Fig 9 revealed that a 900 Hz oscillation develops around the time t = 4.05 sec, which increases in frequency to 1.3 kHz at t = 4.3 sec, and then slows down and disappears at 4.4 sec. The time expanded traces in Fig. 13 show that the oscillations of the two central traces (R = 2.47 and 2.68 m) have the same phase, whereas further out at R= 2.23 m and at 3.00 m, the phase is shifted 180° with respect to the central traces. This indicates that the instability has an even poloidal mode number, and Mirnov coil measurements have confirmed that it is an m = 2, n = 1 mode. On the outer collimator traces, there is unfortunately so much neutron shot noise that we do not obtain reasonable signals from the MHD instability. On an X-ray imaging diagnostic, one usually would see another 180° phase flip at the location of the magnetic island of the tearing instability, i. e. on the q=2 magnetic surface.

The inverted neutron sawteeth are seen later in the same discharge in the time period from 4.6 to 4.75 sec. A time expansion of this tome period is shown in the lower graph of Fig. 12. The inverted sawteeth are most prominent on the traces at R= 2.08 m and at 2.23 m. The neutron line density in the central channels (R = 2.47 and R= 2.68 m) clearly goes up during the events - although at a comparatively small relative rate - whereas the intensity at R=2.23 m and 3.00 m decreases. Quite curiously, there exists a further inversion of the sawtooth at radius R =2.08 m. One possible explanation could be that a partial reconnection at approximately a major radius of R = 2.10 m leads to an accel-

eration of hot ions in the central region, resulting in an increase of the central neutron emission. However, this is only speculation at the present time. The inverted sawteeth were found only in this one discharge, shot #79092, and they did not show up on the ECE emission.

As a last example for the wave detection capabilities of the neutron collimator, we discuss a major disruption that occurred during shot #76778, the shot with highest fusion power (9.3 MW) during the second phase of tritium operation in TFTR. A detailed analysis of this disruption involving all diagnostic evidence has been performed in Ref. 26. The traces for the neutron collimator are shown in Fig. 14. The disruption began at time 3.9515 sec. It terminated the discharge and led to a complete loss of the hot ions in 2.5 msec. The time expanded traces in Fig. 14 show that the disruption proceeded in two phases, which are indicated in the figure by hatching. During the first phase a minor disruption occurred. The intensity in the central channels, i.e. at R = 2.47, 2.68, and 3.00 m, decreases, whereas the intensity in the other traces increases. Apparently, hot ions are expelled from the plasma core, ending up in the outer plasma region during this phase. Similar minor disruptions are observed frequently on TFTR. Often they have a m=1, n=1 precursor, and are very similar to sawteeth except that the reconnection does not seem to be complete. Sometimes the minor disruptions have a 4/3 or a 3/2 precursor. The precursors can often be observed on the neutron collimator, and it can be determined whether the mode is odd or even from the phasing. However, in this case (shot #76778), a precursor and its phase relationships could not uniquely be identified, although the trace at R = 2.47 m suggests that there was an 8 kHz, probably odd, precursor. There is a clear n=1 precursor visible on Mirnov coils, and an odd mode at the same frequency on one of the ECE polychromators[26]. In addition, the ECE polychromators saw a ballooning mode about 1 ms before the onset of the disruption. Usually the plasma recovers fairly rapidly from a minor dis-

ruption. Also in this case the discharge begins to recuperate, and we have a recovery period from 3.95175 sec to 3.9529 sec. The four graphs of Fig. 15 provide a comparison of different diagnostics during that period, that is illuminating. Shortly after the minor disruption, the ECE signal indicates a total collapse of the electron temperature from 10.7 keV to below 2 keV, recovering later to a value in the range 5 to 7 keV. There occurred another short temperature collapse around t = 3.9524 sec, associated with a loss of fusion alpha particles. However, during the whole recovery period, the neutrons, i.e. the fast ion population (which incurred a 20 % decrease during the minor disruption) is hardly affected, - as is the plasma current. The second event, which leads to the final termination of the plasma starts at time 3.9529 sec. Around this time, the electron temperature profile collapses totally, and the hot ion component is severely diminished. The first signs for the second event are neutron signal decreases at R = 2.08 m and R = 3.16 m, and a signal increase at R = 1.94 m. These three channels monitor the outer plasma area, and their behavior is very similar to that found on soft X-ray traces during disruptions involving m=2 or m=3 instabilities. The traces indicate an anomalous transport across a rational q surface, a process that starts locally at that surface and spreads from their inward and outward, affecting finally also the central and the plasma edge regions. At R = 2.08m, after the initial decrease there occurs an increase of the neutron emission which is probably caused by the transport of hot ions from the plasma core. Actually there seem to be two such "transport" events that peak at times 3.532 and 3.5385 sec on the inner collimator channels (R = 1.94 and 2.08 m). The neutron intensity increases perhaps also on the outer channel (R = 3.16 m), although this is not completely clear. Since the increase is much more pronounced on the inner channel, there is a simultaneous inward shift. So far no precursor instabilities for the second event could been identified.

V. Discussion: Implications for future devices.

The NE 451 detector system of the TFTR Neutron Collimator was operated in the current mode. The improved time resolution allowed us to use the neutron collimator as a wave detector for MHD instabilities, and many MHD phenomena were observed on neutron collimator traces for the first time. However, there is still a considerable background of noise on the traces, which prevents us from obtaining results that are truly equivalent to the data obtained with X-ray imaging arrays or with ECE polychromators. The analysis in Section III shows that the noise is neutron shot noise. Small improvement should be obtainable by using more efficient detectors. However, since the noise figure for the present NE451 system is around 4, better detector efficiency will not yield much more than a factor of 2 or 3 improvement. In principle, much larger improvements can be obtained by increasing the detector area through an extension of the collimator channel in the toroidal direction (which is an ignorable coordinate). For instance, providing a collimator channel with a 5 cm $\times$ 25 cm slot opening instead of the present 5 cm diameter opening, should yield a reduction in noise by a factor of 5. A collimator with these properties may be hard to implement now on TFTR, but it should clearly be envisioned and planned for future tritium burning tokamaks like TPX[27] or ITER[28].

Acknowledgments: The support of D. Johnson and K. Young is gratefully acknowledged. Cris Barnes' and Steve Sesnic's guidance and help in the calibration of the neutron generator with aluminum activation foils were invaluable. J. Gorman, T. Holoman, and H. Murphy, provided excellent technical assistance. We thank J. Gavrushenko and R. Gernhardt for "dusting up" the PLT X-ray imaging amplifiers. This work has been supported under Department of Energy Contract No. DE-AC02-76-CHO-3073.

References

1 A. L. Roquemore, R. C. Chouinard, M. Diesso, R. Palladino, J. D. Strachan, and G. Tait: Rev. Sci. Instrum. **61**, 3163 (1990).

2 L. C. Johnson: Rev. Sci. Instrum **63**, 4517 (1992).

3 A. L. Roquemore, L.C. Johnson, and S. von Goeler: Rev. Sci. Instrum. **66**, 916 (1995)

4 R. J. Hawryluck, H. Adler, P. Alling, C. Ancher, H. Anderson, et al.: Plasma Physics and Nuclear Fusion Research, Proc of the 15th Intern. Conf. Seville (Spain), 1994 (International Atomic Energy Agency, Viennna, 1994) IAEA-CN-60/A-1-I-1

5 K. L. Wong, R. J. Fonck, S. F. Paul, D. R. Roberts, E. D. Fredrickson, et al.: Phys. Rev. Lett. **66**, p. 1874 (1991)

6 W. W Heidbrink, E. J. Strait, E. Doyle, G. Sager, and R. Snyder: Nucl. Fusion **31**, p. 1635 (1991)

7 R. V. Budny, M. G. Bell, D. K. Mansfield, J. D. Strachan, S. Zweben: Proc. 21st EPS Conf. on Contr. Fusion and Plasma Physics (Montpellier, France) Part 1, p.82 (1994).

8 Z. Chang, E. D. Fredrickson. J. D. Callen, K. M. McGuire, M. G. Bell, et al.: Nucl. Fusion 34, p. 1309 (1994).

9 L. C. Johnson, P. C. Efthimion, J. D. Strachan, E. Synakowski, M. Zarnstorff, et al.: Proc. 21st EPS Conf. on Contr. Fusion and Plasma Physics (Montpellier, France) Part 1, p.182 (1994)

10 Manufactured by NUCLEAR ENTERPRISES Inc., San Carlos CA 94070

11 K. W. Hill, S. von Goeler, M. Bitter, W. Davis, L. Dudek et al.: Rev. Sci. Instrum. 56, p. 830 (1985)

12 J. D. Strachan, C. W. Barnes, M. Diesso, D. Jasby, L. C.Johnson et al.: Rev. Sci. Instrum. **66**, p.897, (1995)

13 M. Osakabe, J. Fujita, J. Kodeira, M. Sasao, H. Yamanishi, et al..: Rev. Sci. Instrum. **66**, p.: 920 (1995)

14 Long Poe Ku: private communication.

15 S. O. Rice: "Mathematical Analysis of Random Noise" in 'Noise and Stochastic Processes', N. Wax Editor, Dover Publications ,New York, p.133, (1954).

16 14 MeV Neutron Generator Model 320, MF Physics Corporation, Colorado Springs, Colorado 80919.

17 A. L. Roquemore, D. L. Jasby, L. C. Johnson, and J. D. Strachan, and C. W. Barnes: Proc. 15th IEEE Symposium on Fusion Energy, Hyannis MA, Vol. I, p. 114 (1994).

18 C. W. Barnes, A. R. Larson. G. LeMunyan, and M. J. Loughlin: Rev. Sci. Instrum. **66**, p. 888 (1995).

19 S. von Goeler, W. Stodiek, and N. Sauthoff: Phys. Rev. Lett. **33**, p.1201 (1974).

20 G. Jahns, M. Soler, S. V. Wadell, J. Callen, and H. Hicks: Nucl. Fusion **18**, p. 609 (1978)

21 E. D. Fredrickson, A. C. Janos, K.. M.. McGuire, S. D. Scott, G. Taylor, and Z. Chang: Nucl. Fusion **33**, p 1759 (1993).

22 K. McGuire, et al..: Phys. Rev. Lett. **50**, p891 (1983)

23 R. Kaita, R. B. White, A. W. Morris, E. D. Fredrickson, K. M. McGuire et al.: Phys. Fluids B **2**, p.1584 (1990)

24 R. White, R. Goldston, K. McGuire, A. Boozer, D. Monticello, and W. Park: Phys Fluids **26**, p2958 (1983).

25 L. Chen, R. B. White, and N. M. Rosenbluth: Phys. Rev. Lett. **52**, 1122 (1984)

26 S. Mirnov, I. Semenov, E.Fredrickson, R. Budny, K. McGuire et al.: "Phenomenology of major disruptions in high b DT TFTR plasmas", to be published.

27 S. S. Medley: Rev. Sci. Instrum. **66**, p. 297 (1995)

28 A. E. Costley: Rev. Sci. Instrum. **66**, p. 296 (1995)

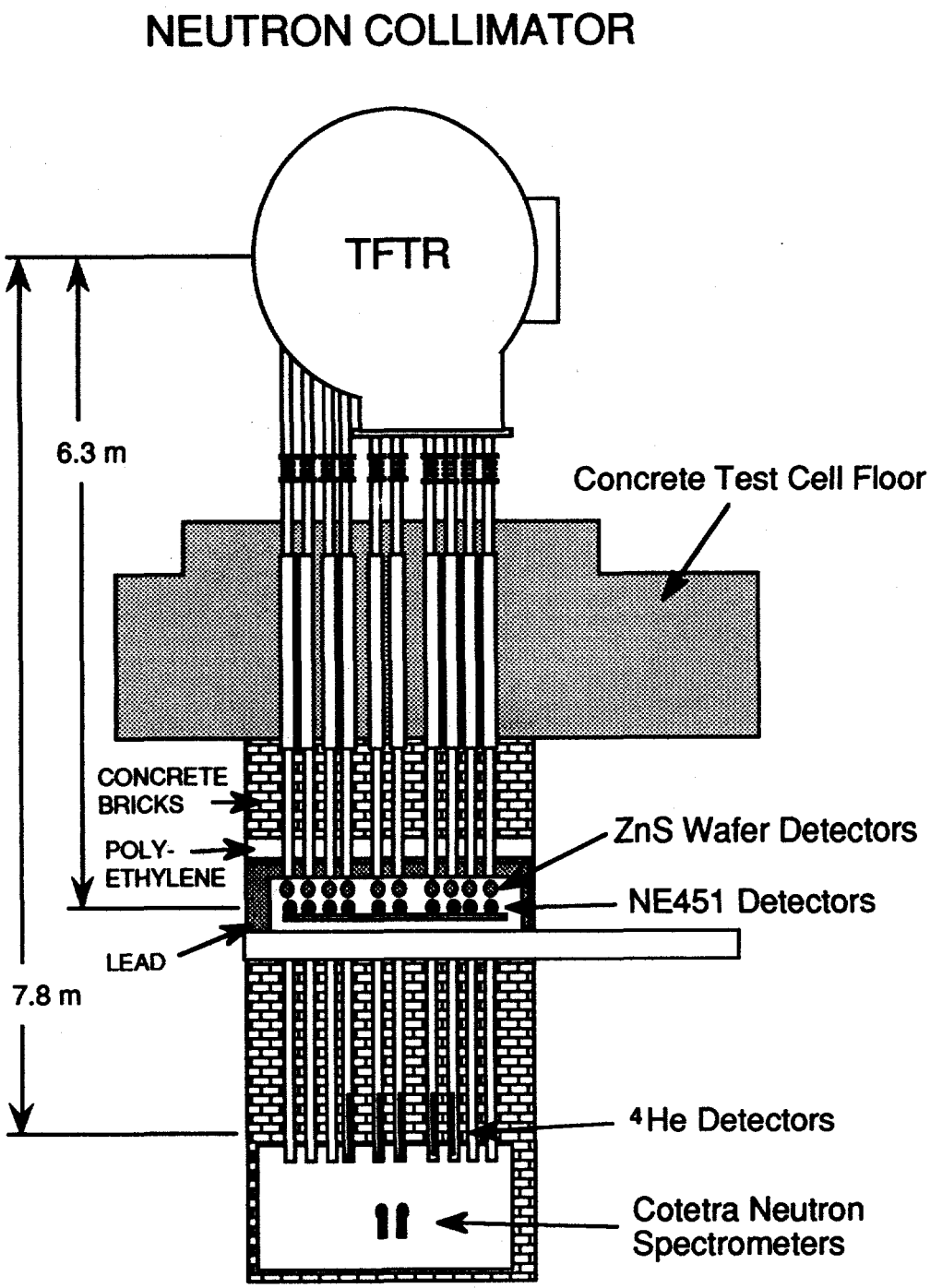

Fig. 1: Mechanical layout of the Neutron Collimator.

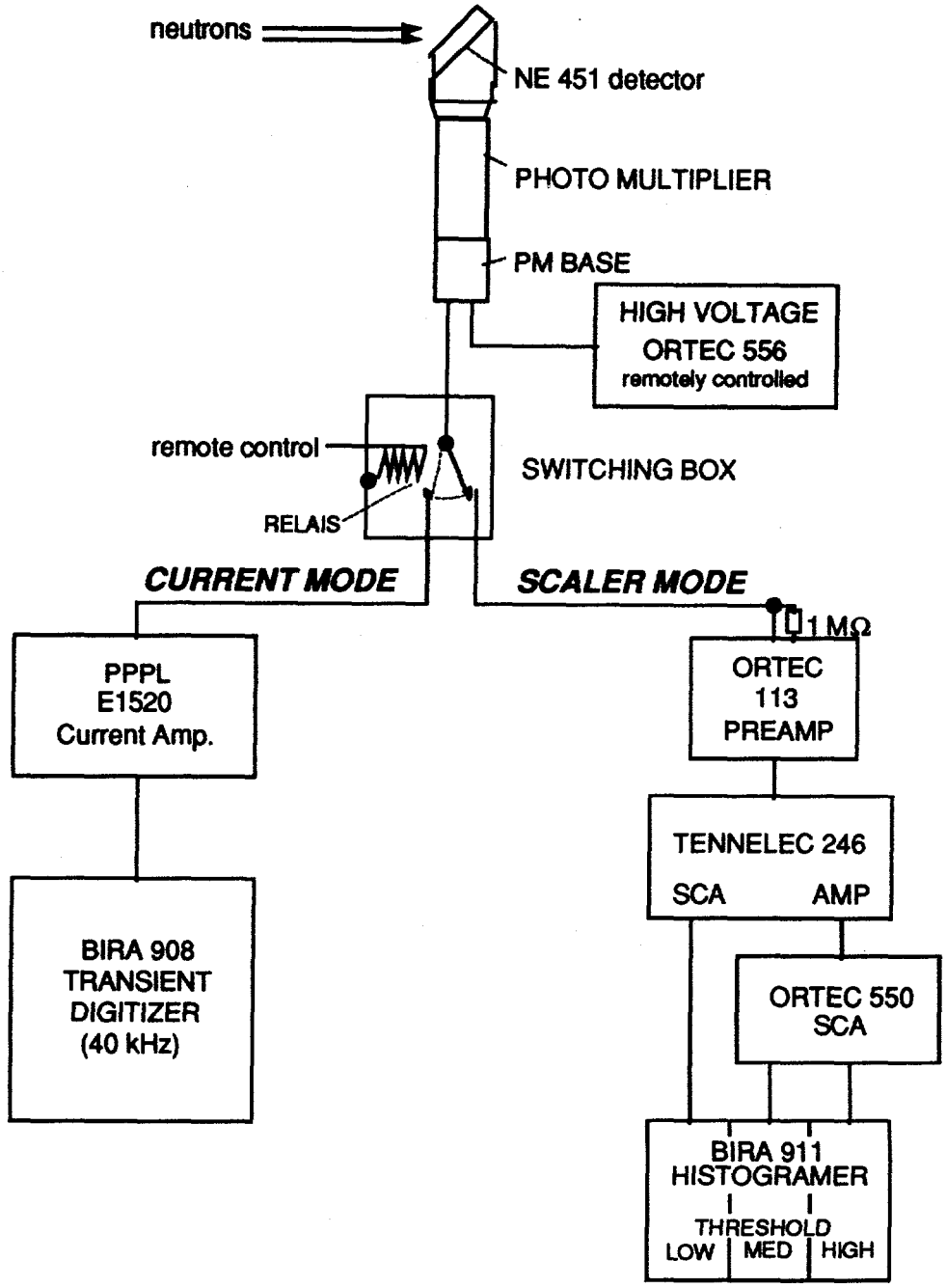

Fig. 2: Signal processing electronics for the current mode of operation.

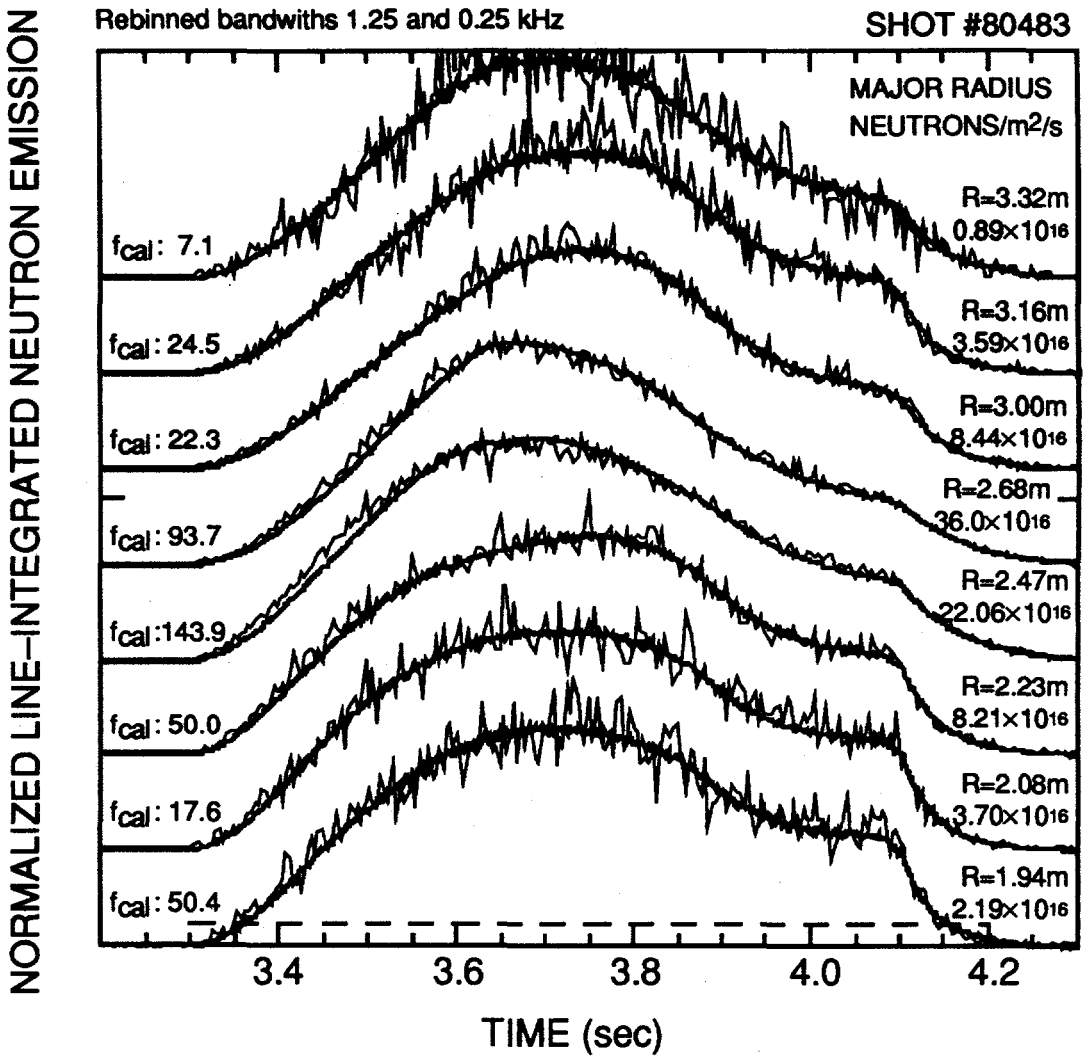

Fig. 3: Calibration of the current mode signals. Thick solid lines: Signals from the NE 451 detectors in current mode. All signals are normalized to 1. The value for maximum of the chord integrated neutron emission for each trace is shown on the right side of the graph where the signal goes to zero. Thin solid lines: Signals from the ZnS wafer detectors in pulse counting mode. The current mode traces were multiplied with a calibration factor fcal, which was obtained by dividing the average of the wafer detector signal by the average of the Ne451 current mode signal. The averaging was performed in the time interval indicated by the dashed horizontal line.

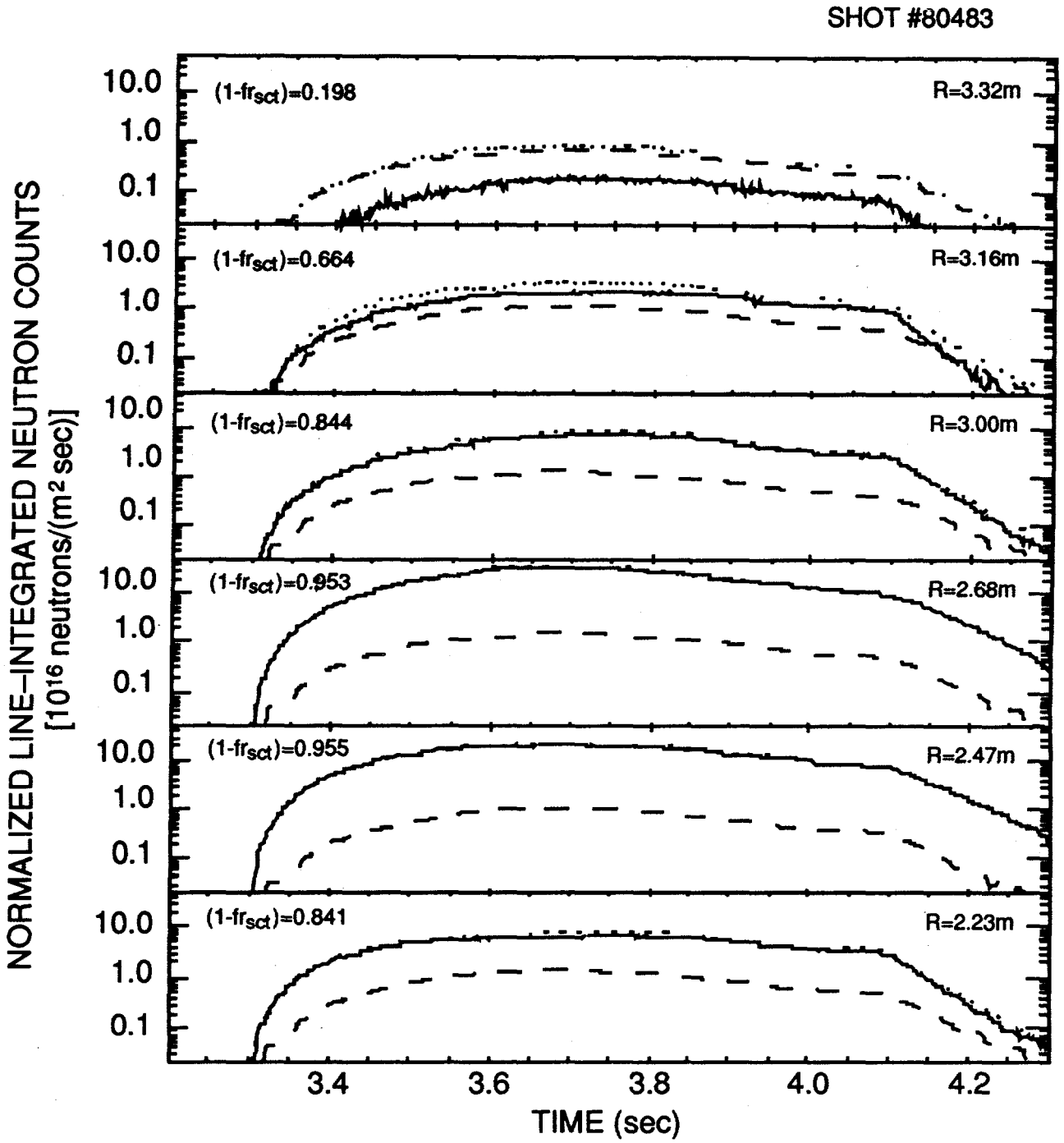

Fig. 4: Scattered Neutron Correction. The raw, highly-smoothed current-mode signals are represented by the dotted curves. The dashed curves shows the scattered neutron contribution, which is derived from a general neutron signal (i. e. the fission chamber NE-CU-S3). The dashed curves are subtracted from the corresponding dotted curves. The result (solid curves) is a set of corrected traces for the chord integrated neutron emission .

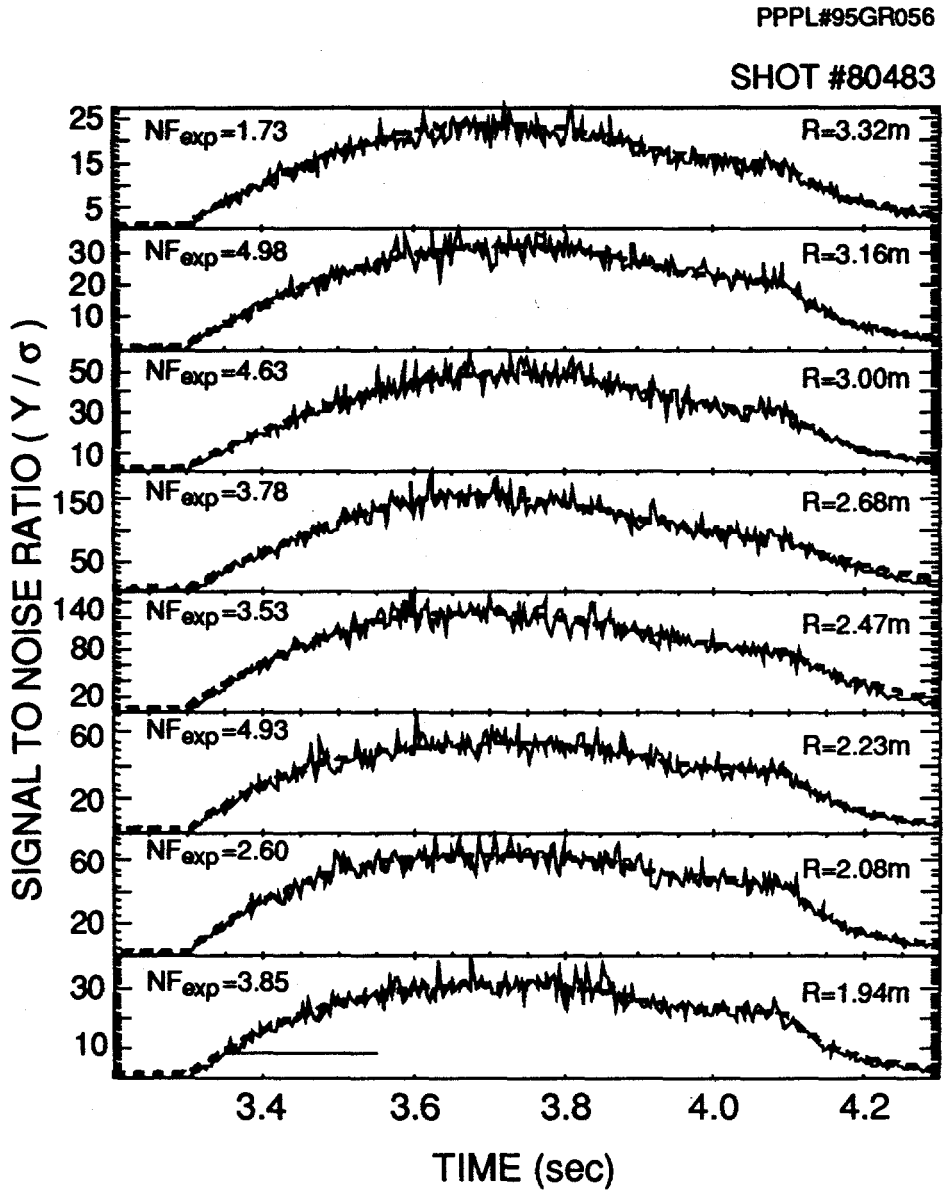

Fig. 5: Signal to noise ratio. The thin solid curves represent the measured signal to noise ratio, referred to as SNR_{exp} in the text.. The heavy dashed lines represent calculated noise, i.e. the quantity $SNR_{nsn} \times NF_{exp}$. The experimental noise factor NFexp was obtained by normalizing the two curves to fall on top of each other in the time interval indicated by the thin solid horizontal line.

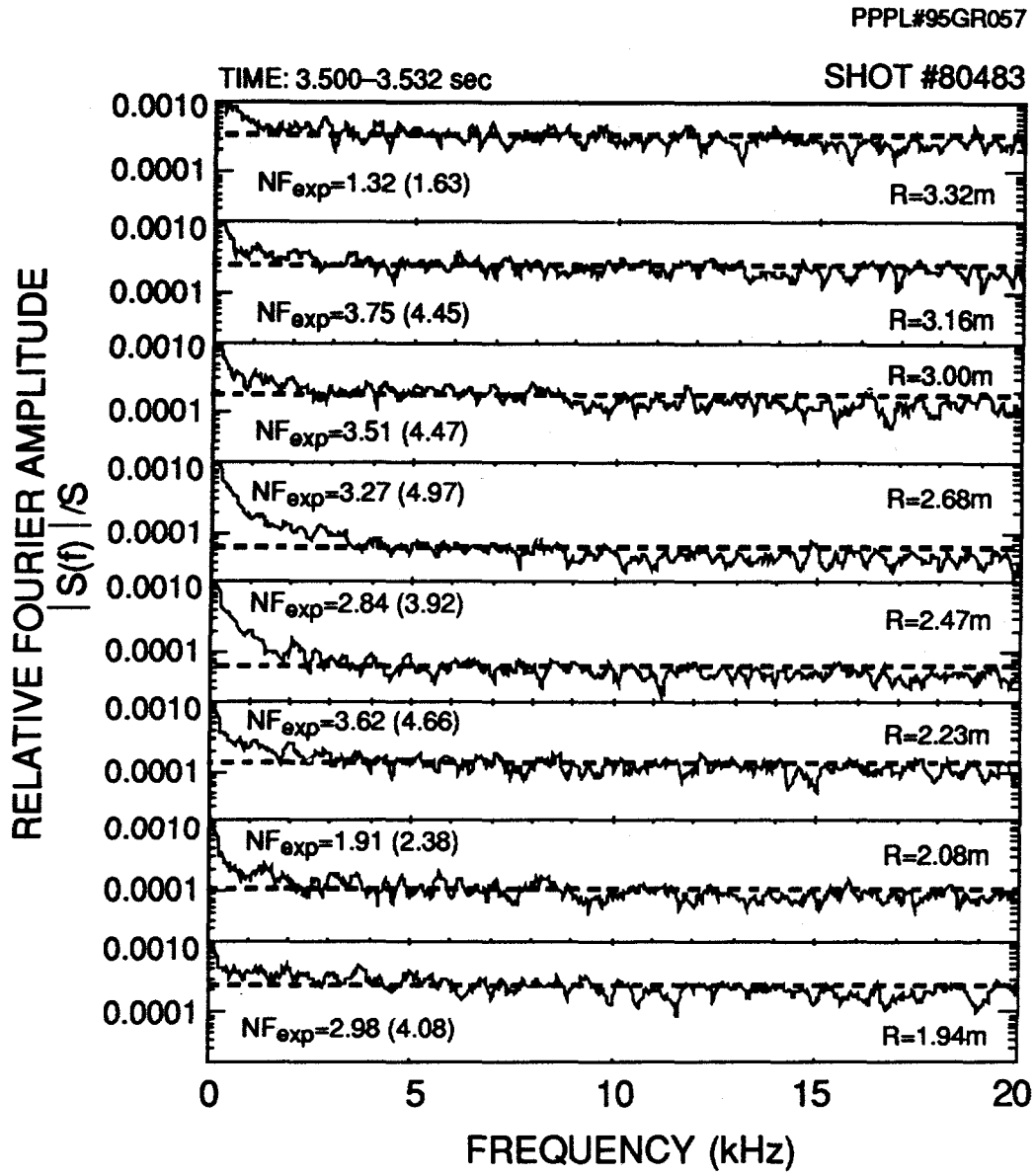

Fig. 6: Fourier spectra during a MHD-free period. The thin line represents the fast Fourier transform of the current mode traces in the specified time interval. The heavy dashed lines represent calculated neutron shot noise spectra, i. e. the quantity $FT_{nsn} \times NF_{exp}$. The quantity NF_{exp} was obtained by fitting the two curves to each other in the frequency interval from 1.88 - 20.0 kHz. The value in brackets are for a fit in the frequency interval 1.88 - 5.0 kHz.

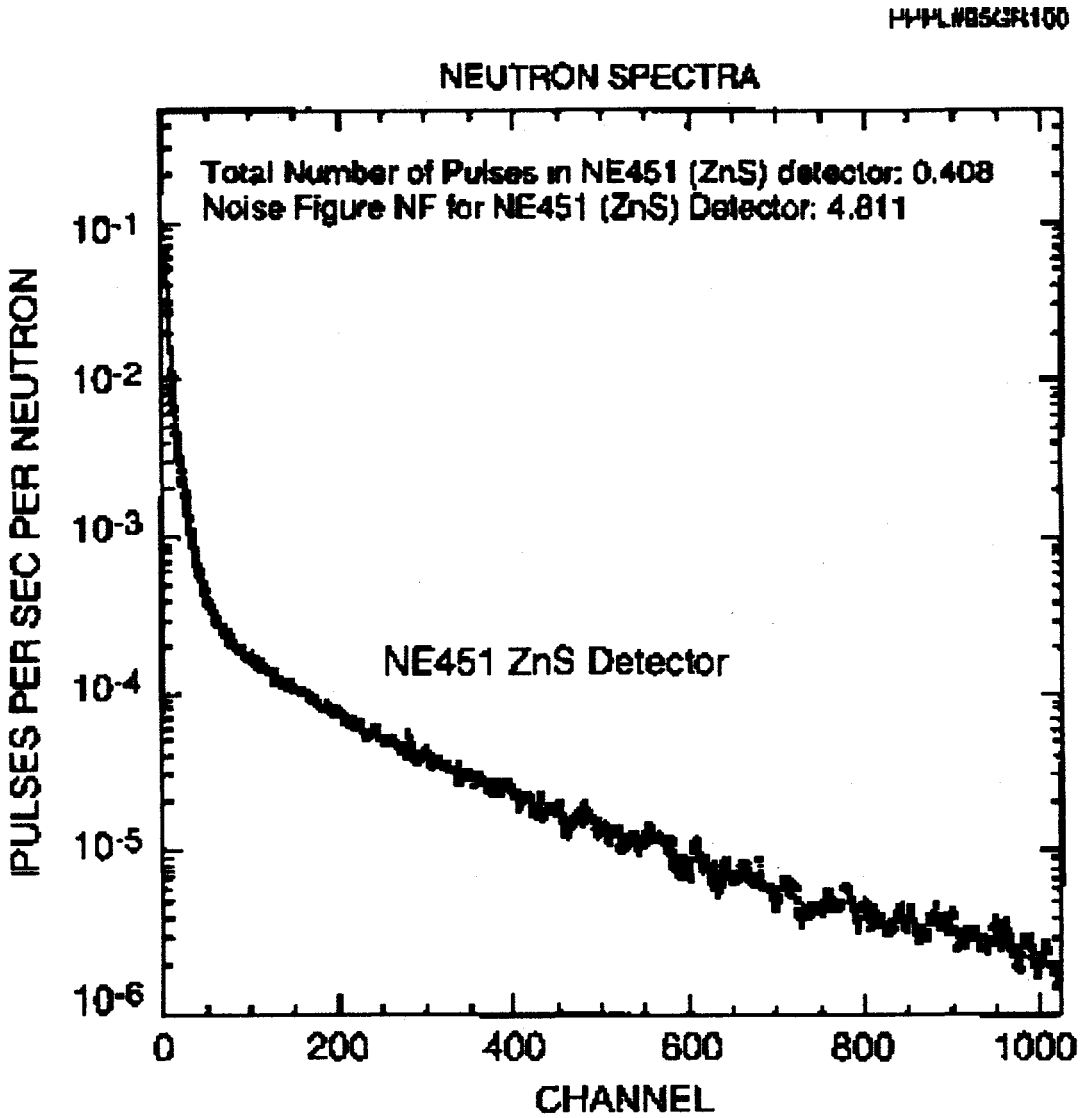

Fig. 7: Pulse height spectrum of a NE451 detector produced by 14 MeV neutrons from a neutron generator. Plotted is the number η of pulses per channel per 14 MeV neutron that passes through the detector. The neutron generator was calibrated with Al activation foils.

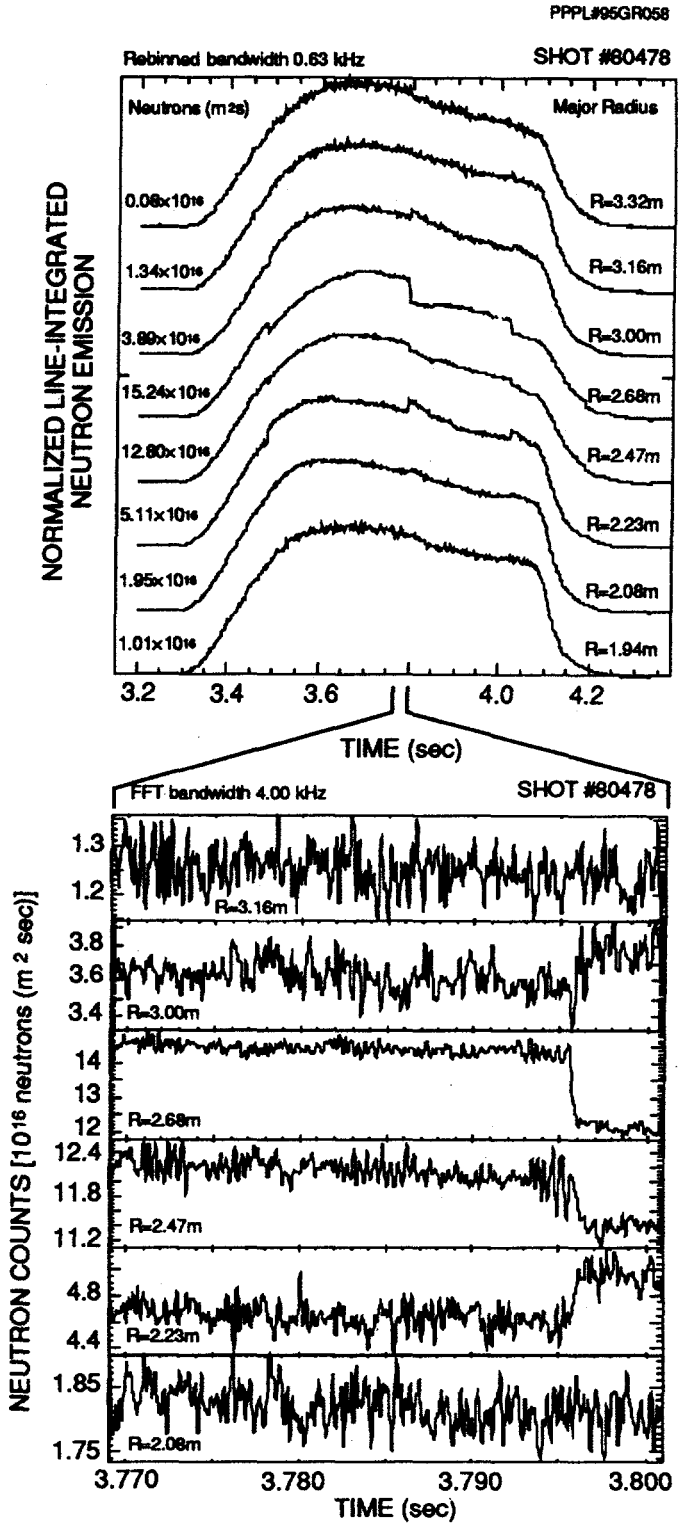

Fig. 8: Neutron collimator current-mode traces in a discharge with sawteeth instabilities. The traces are normalized to 1, the value of the maximum of each trace is given at the left side of the graph. The lower graph shows a time expanded view of the large sawtooth at 3.795 sec. Fishbone precursor instabilities are clearly visible, in particular on the trace at R=2.47 m.

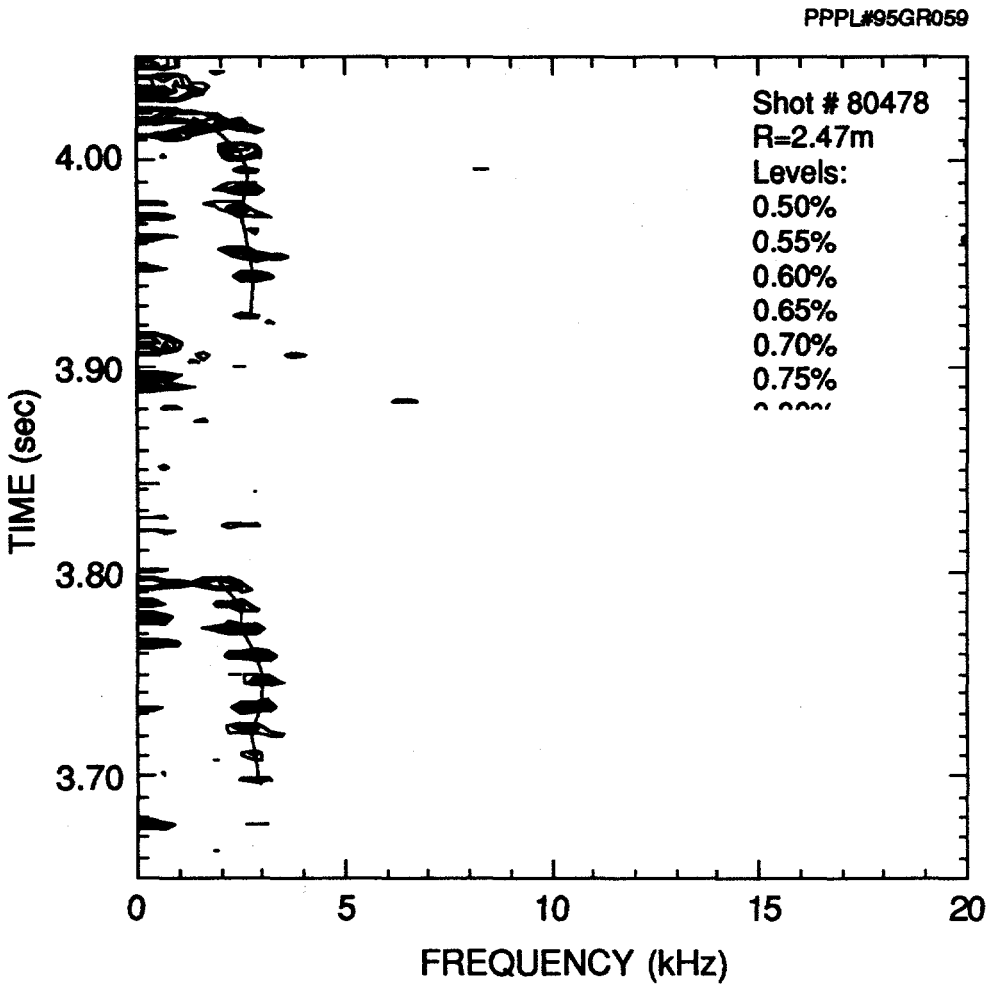

Fig. 9: Contour plot of fast Fourier spectra versus frequency and time. The spectral analysis is performed every 3.2 ms. The fishbone instabilities show up in the frequency range 2 - 3 kHz in the time ranges 3.7 -3.8 sec and 3.92- 4.2 sec. The maxima of the fishbone amplitude have been connected by a thin line in order to demonstrate the characteristic slowing down of the m/m = 1/1 frequency before a sawtooth.

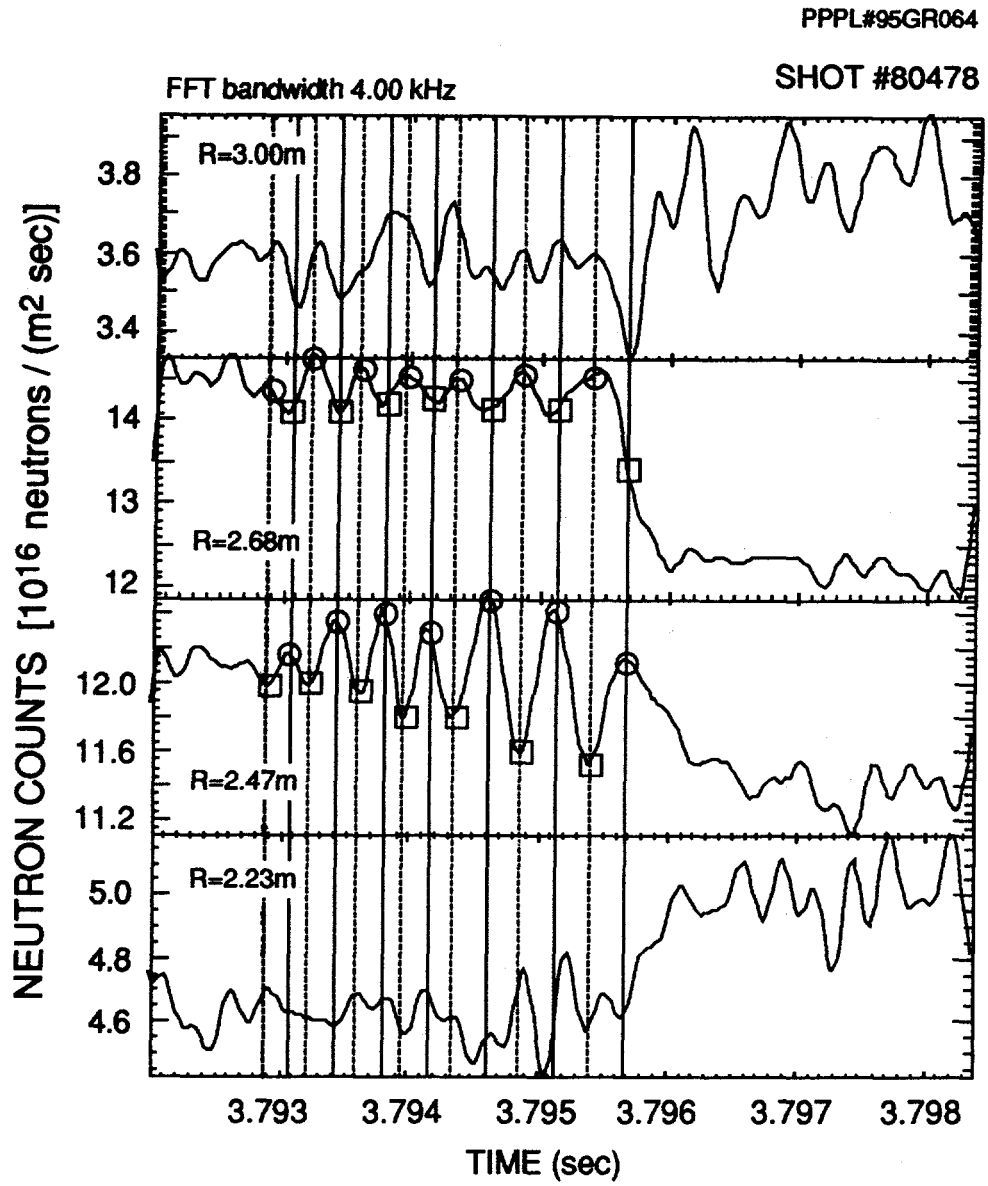

Fig. 10: Precursor of the sawtooth instability. The four central traces of the neutron collimator are shown in a very expanded view directly before the sawtooth crash. The maxima of the precursor are indicated by circles and the minima by squares. The maxima for R = 2.68 m occur at the time of the minima for R = 2.47 m, showing that the precursor is an odd mode.

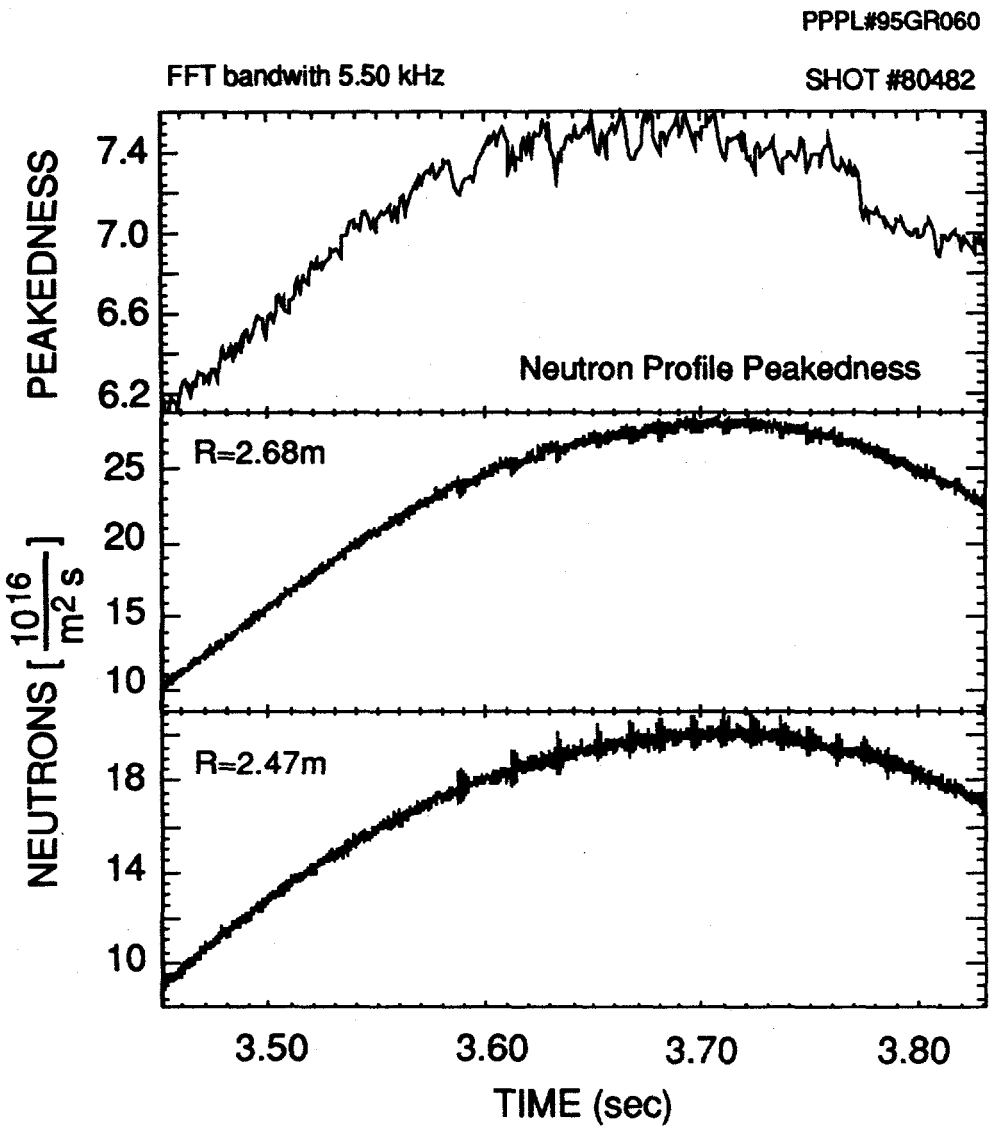

Fig. 11: Effect of fishbone instabilities on neutron emission profiles. Plotted are the neutron peakedness and the two central collimator traces during the onset of fishbone instabilities. Each one of the fishbone instability bursts - clearly visible on the trace for R=2.47 m - is associated with a tiny sawtooth on the trace at R = 2.68 m, an tiny inverted sawtooth on the trace at R=2.47 m, and a sudden loss of neutron peakedness.

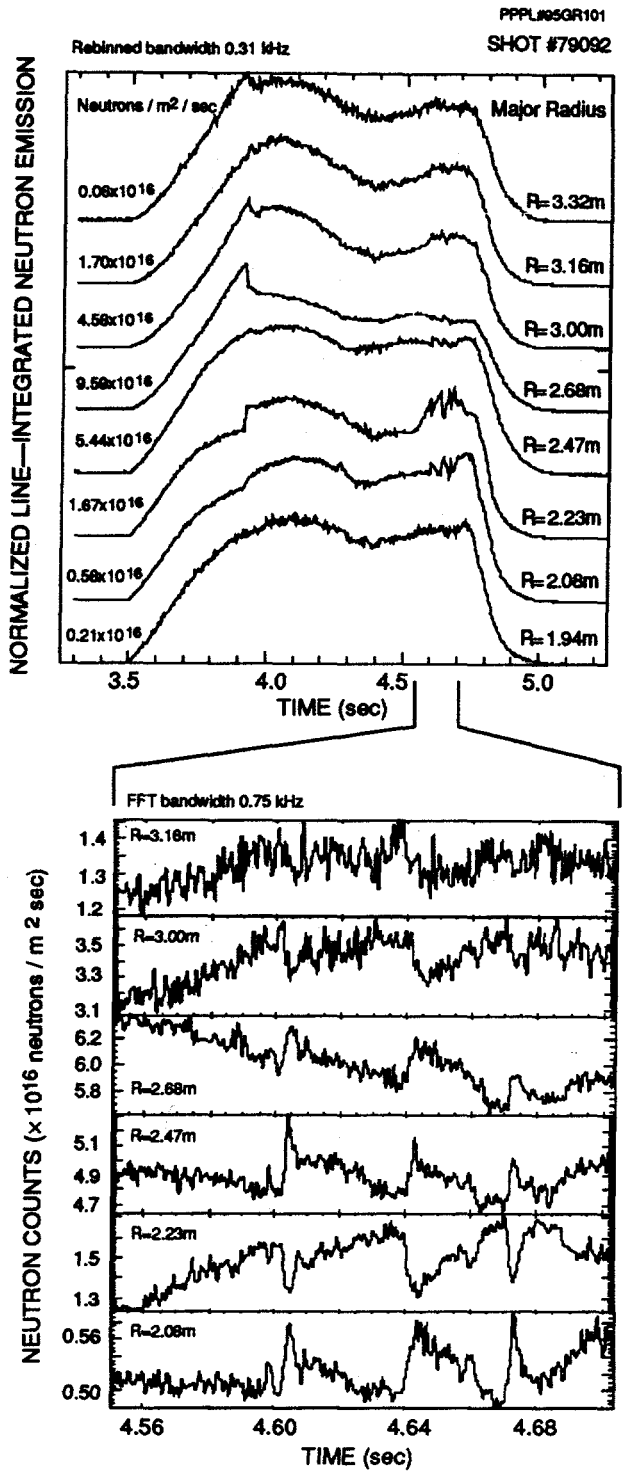

Fig. 12: Neutron collimator traces for TFTR shot #79092. The traces exhibit inverted neutron sawteeth, shown in the time expanded lower graph., and a continuous 900 Hz m/n = 2/1 oscillation during the time period from 4.0 to 4.3 sec, shown in Fig. 13.

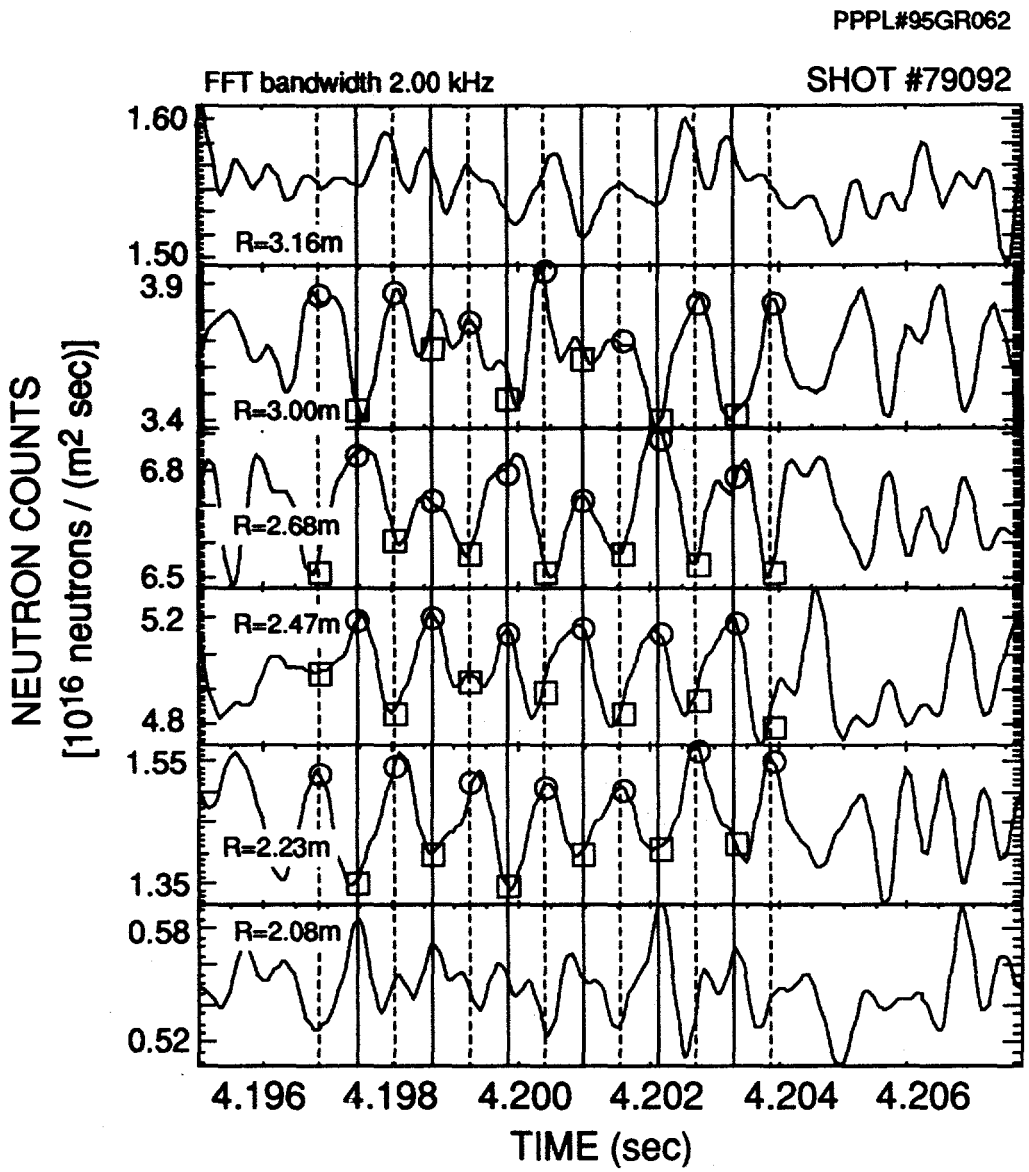

Fig. 13: Phasing of the continuous m/n = 2/1 mode of shot #79092. Maxima and minima of the oscillation are indicated by circles and squares, respectively. The collimator data show that the mode is even.

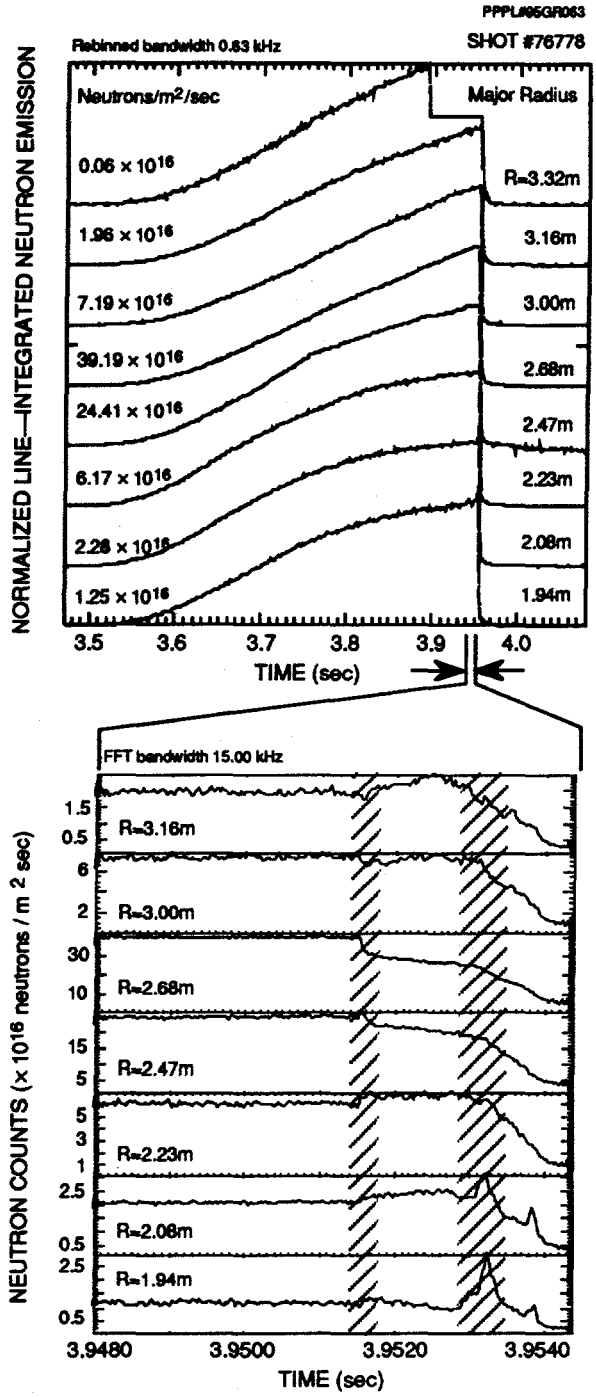

Fig 14: Development of the neutron emission during the major disruption of shot # 76778. Unfortunately, the digitizer for channel #9 (R = 3.32 m) failed in the time after 3.89 sec. The time expansion in the lower graph, indicates that the disruption has two catastrophic phases, indicated by shading. The first phase consists of a minor disruption that starts near the central core. The second phase, the major disruption proper, originates further out at radius R ≈ 2.0 m.

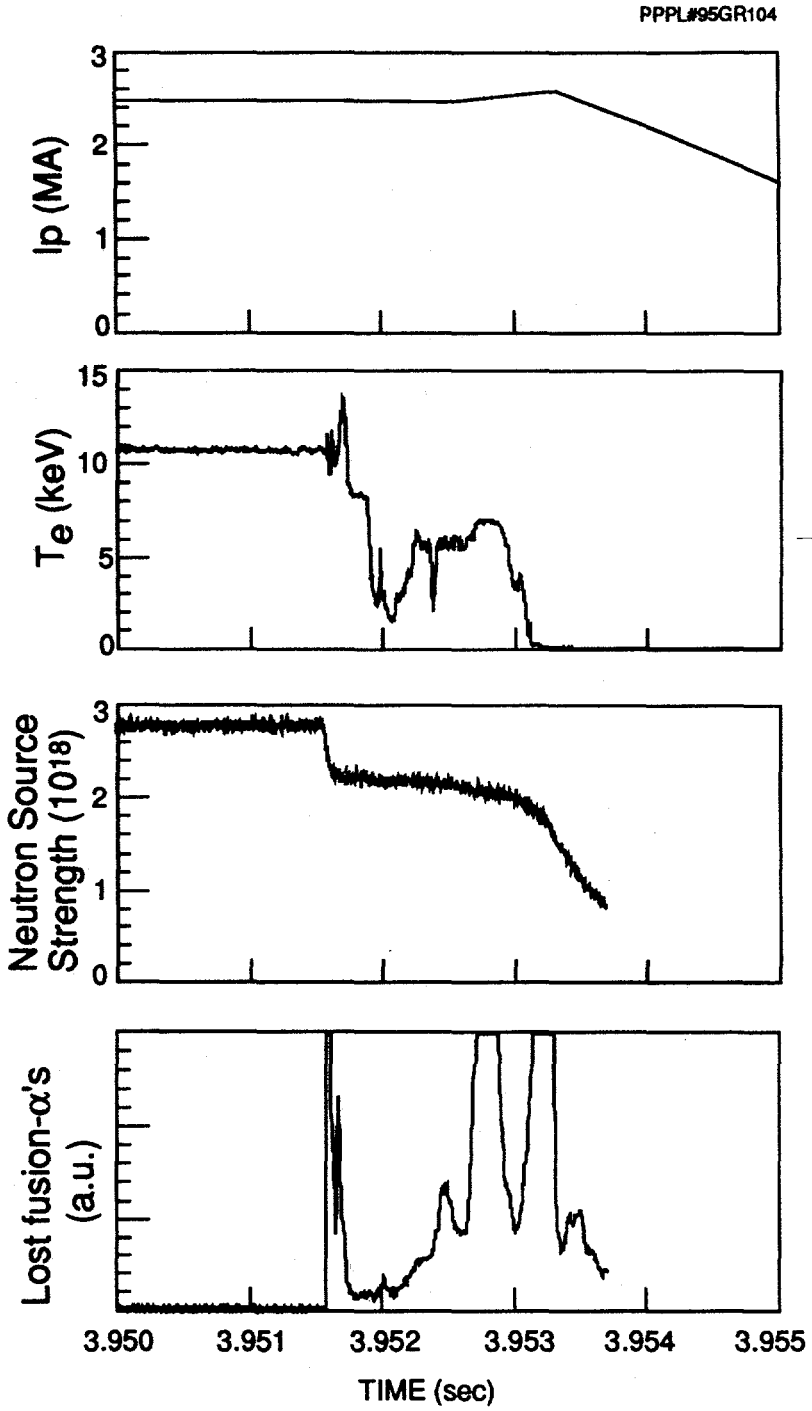

Fig. 15: Major Disruption of shot #76778: Comparison of the time history of the total neutron source strength with the development of the plasma current, the central ECE electron temperature, and the fusion alpha particle loss.

DISCLAIMER

This report was prepared as an account of work sponsored by an agency of the United States Government. Neither the United States Government nor any agency thereof, nor any of their employees, makes any warranty, express or implied, or assumes any legal liability or responsibility for the accuracy, completeness, or usefulness of any information, apparatus, product, or process disclosed, or represents that its use would not infringe privately owned rights. Reference herein to any specific commercial product, process, or service by trade name, trademark, manufacturer, or otherwise does not necessarily constitute or imply its endorsement, recommendation, or favoring by the United States Government or any agency thereof. The views and opinions of authors expressed herein do not necessarily state or reflect those of the United States Government or any agency thereof.